ELSEVIER

Contents lists available at ScienceDirect

Materials Characterization

journal homepage: www.elsevier.com/locate/matchar



Microstructural modification and enhanced mechanical properties in Zr_{50} - Ti_{50} alloy via low temperature electron wind force annealing

Md Hafijur Rahman a, Hajin Oh a, Daudi Waryoba b, Aman Haque a,*

- ^a Department of Mechanical Engineering. The Pennsylvania State University, University Park, PA 16803, USA
- ^b Engineering, Applied Materials, Penn State University, College Place, DuBois, PA 15801, USA

ARTICLE INFO

Keywords: Low temperature electropulsing Zr-Ti alloy Alpha lath structure Electron backscatter diffraction (EBSD) X-ray diffraction (XRD)

ABSTRACT

This study investigates the microstructural transformations and associated property enhancements in a $\rm Zr_{50}\text{-}Ti_{50}$ alloy annealed at only 120 °C with low duty cycle current pulses. Microanalysis with electron backscatter diffraction (EBSD) and X-ray diffraction (XRD) show the formation of alpha lath structure, typically observed in much higher thermal annealing temperatures. EBSD and XRD analyses revealed the formation and/or growth of the lath structure, with notable changes in pole distributions and the appearance of a distinct peak at 52.5° in the XRD spectrum. The lath structure is quantified using FiJi weka segmentation machine learning technique. Nanoindentation data showed an increase in the average hardness from ~7 to ~8 GPa and a corresponding increment in the reduced modulus from 127 to 148 GPa. The observed increase in low-angle grain boundaries (LAGBs) from 4% to 12% further complements the findings, suggesting a complex interplay of microstructural features contributing to the overall improvement in the mechanical properties. The proposed low temperature annealing technique demonstrates the predominant role of the electron wind force for tailoring the microstructure and mechanical performance of Zr—Ti alloys, providing insights that could have implications for the broader field of materials engineering.

1. Introduction

Zirconium-titanium (Zr-Ti) alloys stand as pivotal materials in various high-performance applications, such as aerospace, biomedical and nuclear industries, owing to their exceptional dimensional stability, high temperature strength, and appropriate stiffness [1-3]. Conventionally, the production of Zr-Ti alloys involves processes like the selfconsumption arc furnace melting method, wherein the alloy composition is achieved by melting an electrode with desired constituents through a vacuum arc [4.5]. Alternately, spark plasma sintering (SPS) method rapidly densifies materials by integrating plasma activation, resistance heating, and hot-pressing sintering, offering advantages such as reduced processing time and lower temperatures compared to the self-consumption arc furnace melting method [6-8]. The resulting alloy typically exhibits a mixture of beta (β) and alpha (α) phases at room temperature, with the alpha phase being dominant [8,9]. To optimize the mechanical properties of Zr—Ti alloys, heat treatment processes like annealing have been widely employed [10-12]. Annealing involves heating the alloy to temperatures within the beta phase stability range. The alloy is held at this elevated temperature to allow for homogenization and nucleation of the alpha phase, followed by controlled cooling to induce a phase transformation from beta to alpha [10-12]. The transformation from beta to alpha phase depends on multiple factors, such as the temperature at which annealing is performed, the holding time and cooling rate [12]. During this transformation, needle-like elongated alpha lath structure is formed for some particular conditions. The formation of alpha lath structure, characterized by its elongated and acicular morphology, contributes to the alloy's enhanced strength and hardness [6,13]. Thus, understanding the formation of lath structure is essential for optimizing the performance of these alloys. For example, Liu et al. [12] have shown that alpha lath structure is formed during the annealing of Zr—Ti alloy at 400-500 °C with lower holding time and faster cooling rate. This phase transition temperature depends on the alloy composition and their relative percentage [14]. The addition of oxygen significantly increase the alpha/ beta transition temperature and works as alpha phase stabilizer [15]. Domagala et al. [16] have shown that the alpha/beta transition temperature is more than 900 °C for a Ti-Zr-O system, meaning that, to form lath structure in this alloy system by thermal annealing, at least 900 °C temperature is required. Moreover, traditional annealing methods lead

E-mail address: mah37@psu.edu (A. Haque).

^{*} Corresponding author.

to potential drawbacks such as grain coarsening, increased energy consumption, and non-uniform changes in microstructure across the material [17,18]. In response to these challenges, an innovative approach involving the utilization of electropulsing is proposed as an alternative to conventional annealing. For instance, Park et al.'s [19] finding suggests that lower annealing temperatures and shorter annealing times are needed in electropulsing treatment (EPT) compared to heat treatment.

Electropulsing, characterized by short pulse width and lowfrequency current pulses, provides a unique avenue for microstructural manipulation in alloys [20-23], typically in a very short time. Zhu et al. [20] have observed recrystallization in cold-rolled TiNi alloy within 9 s and achieved maximum super-elasticity by controlling electropulsing parameters and grain size. Electropulsing has also been used to enhance plastic elongation in a cold-deformed Zn—Al alloy (ZA22) by inducing circular phase transformations, improving dislocation identities, and influencing microstructures [24]. Yang et al. [25] investigated the microstructural evolution and mechanical properties of a deformed Zr-Ti-Al-V alloy after electropulsing treatment and showed that a charging voltage of 2 kV induces a slight decrease in dislocation density due to the electron wind, softening the alloy despite a peak temperature of only 86 $^{\circ}$ C. They further observed that increasing the voltage to 6 kV elevates the temperature and accelerates the $\alpha'' \to \beta \to \alpha$ phase transformation, which strengthen the alloy significantly [25].

In this study we investigate the response of a Zr—Ti alloy under the application of low temperature electropulsing. Unlike conventional thermal annealing, electropulsing imparts controlled electrical pulses to the material, inducing changes in its structure and behavior. The microstructural change is a result of simultaneous effect of thermal (joule) heating induced by high current density and electron wind force [26-29]. For example, Kim et al. [28] have shown that electric current can indeed have a distinct role in inducing annealing, separate from the effects of Joule heating. It is to be noted that the conventional electropulsing can induce temperature of 600-1000 °C, which makes the thermal force as a dominant factor for the microstructural change [25]. In this study we keep the temperature rise around 100 °C by controlling the pulse width, current density and frequency. This low temperature electropulsing makes the electron wind force a significant factor along with thermal force in altering the microstructure of materials, as indicated in our previous publications [30-32]. As mentioned earlier, the presence of oxygen makes the formation of lath structure by thermal annealing energetically unfavorable (required temperature is 800–1000 °C), this study demonstrate that the alpha lath structure can be induced at significantly lower temperatures (120 °C) through carefully controlled electropulsing. To comprehensively evaluate the

material's response to electropulsing, electron backscatter diffraction (EBSD) and X-ray diffraction (XRD) analyses were conducted for various electropulsing conditions. Additionally, nanoindentation experiments were conducted to provide quantitative insights into changes in mechanical properties, specifically hardness and reduced modulus. The implications of this research extend beyond the immediate focus on Zr—Ti alloy, opening avenues for innovative approaches in controlled microstructural evolution and property enhancement.

2. Experimental details

In this experimental investigation, we focused on the electropulsing treatment of a Zr-Ti alloy, with a detailed exploration of microstructural changes and potential phase transformations. We bought the Zr—Ti alloy sample from MSE supplies LLC. The energy-dispersive X-ray (EDX) analysis have shown that a contamination of Oxygen (O), Aluminum (Al) and Hafnium (Hf) is present in the alloy (see Fig. 1) and the composition is 62.2%Zr, 32.2%Ti, 3.92%O, 0.3%Al, 1.44%Hf. Electropulsing was performed by applying short pulse width and lowfrequency current pulses, with the concurrent monitoring of the sample temperature using an Optris-PI 600 thermal microscope. To prepare the alloy for detailed microstructural analysis, a multi-step sample preparation approach was implemented. Mechanical polishing using a rotary tool, coupled with diamond polishing compounds, ensured an initial surface refinement. Subsequently, ion milling, operating at 4.5 kV and 1.5 A for a duration of one hour, improved the sample's surface quality, paving the way for subsequent electron backscatter diffraction (EBSD) investigations. EBSD mapping was conducted at three distinct stages. Initially, an EBSD map was obtained from the pristine sample. Subsequently, electropulsing was applied, allowing the sample temperature to rise up to 40 °C, and a second EBSD map was acquired. A second round of electropulsing with a higher current density was then performed, allowing the sample temperature to reach 120 °C, followed by another EBSD mapping session. The detailed electropulsing

Table 1Parameters used in electric processing.

Frequency (Hz)	Pulse width (μs)	Current density $(\frac{A}{cm^2})$	Temperature (°C)	Time (minutes)
2	40	1.94×10^4	40	1
2	40	2.19×10^4	65	1
2	40	2.7×10^4	87	1
2	40	3.37×10^4	115	1
2	40	3.55×10^4	120	1

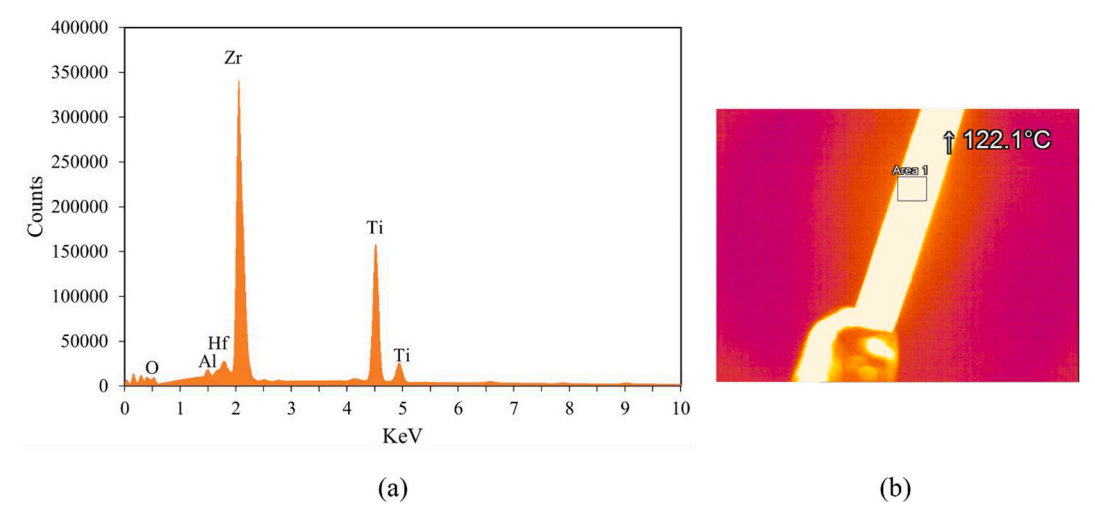


Fig. 1. (a) EDX spectrum confirming the elemental composition, (b) thermograph showing the maximum temperature attained during the electropulsing processing.

parameters are shown in Table 1. During EBSD mapping, a beam current of 3.2 nA and a voltage of 20 V were employed to ensure precise data acquisition. The obtained EBSD data underwent thorough postprocessing analysis using the AztecCrystal software suite to extract meaningful insights into microstructural alterations [33]. In addition, Xray diffraction (XRD) analysis was carried out to confirm the presence of any newly formed phases resulting from the electropulsing treatment. The X-ray diffraction (XRD) analysis was conducted using a Malvern Panalytical Empyrean® instrument equipped with a copper ($K\alpha 1-2$ = 1.540598/1.544426 Å) long-fine-focus X-ray tube operated at 45 kV and 40 mA. Samples were positioned on a programmable manual phi stage to ensure precise data collection. The incident beam path included iCore® optics fitted with a BBHD® optic with 0.03 rad Soller slits, a 0.2 mm primary and a 0.3 mm secondary mask, and a fixed 1/4° divergence slit. The diffracted beam path incorporated dCore® optics with a 1/4° fixed anti-scatter slit, and 0.04 rad Soller slits. A PIXcel3D® detector was used in scanning line (1D) mode with an active length of 3.3482° with a nominal 2θ step size of 0.0236° and count time of 382 s for a total time of one hour. Peak positions were determined, and phase ID was carried out using Jade® software (version 8.9) from Materials Data Inc. (MDI) and the PDF5 database from the International Centre for Diffraction Data (ICDD). Finally, to assess the change in mechanical properties such as hardness and reduced modulus resulting from these electropulsing treatments, nanoindentation experiments were performed using a Bruker Hysitron TI-980 instrument.

3. Results and discussion

In this section, we present a comprehensive analysis of the microstructural evolution and phase transformations observed in our alloy system. The microstructural evolution was captured using electron backscattered diffraction (EBSD) technique, where subsequent changes in microstructures and crystallographic orientations can be interpreted within the context of the alloy's inherent phase composition.

3.1. Evolution of the microstructure during electropulsing

In examining the microstructural evolution of the Zr—Ti alloy through inverse pole figure in the normal direction (zIPF maps), distinct

microstructural transformations were observed under various conditions. In the pristine state, as depicted in Fig. (2a), the microstructural analysis reveals a composition with minimal lath structures. The absence of extensive lath structures suggests a more homogeneous microstructure. Grain boundaries appear relatively smooth, contributing to the semi-equiaxed and broad-lath appearance in the microstructure. The subtle presence of lath structures, although minimal, hints at the potential for phase transformations that become more pronounced under specific conditions, forming the foundation for subsequent comparative analyses following electropulsing treatments.

Typical microstructures of the Zr—Ti alloys originate from the high temperature transformation of the parent β -phase grains, which have a bcc crystal structure, to the low temperature α -phase grains, which have an hcp crystal structure. Depending on the cooling rate, a mixture of basketweave or colony α -laths, acicular α' (martensite), and retained β phases are formed [8,9]. The phase map obtained from electron back-scattered diffraction (EBSD) reveals that the pristine sample consists of $\sim\!80\%$ α -phase and $\sim\!20\%$ of β -phase (see Fig. 3). Slow cooling results to equaixed/semi-equaixed grains to broader/coarse lath morphology, whereas fast cooling (quenching) results to fine/thin lath or acircular (martensitic) microstructure. The relative fractions of these variants, which are determined by materials processing conditions, affect the

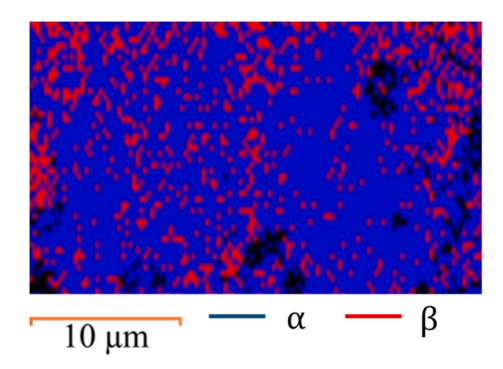


Fig. 3. Pristine phase map obtained from electron backscattered diffraction (EBSD). (The black dots are points of zero solution).

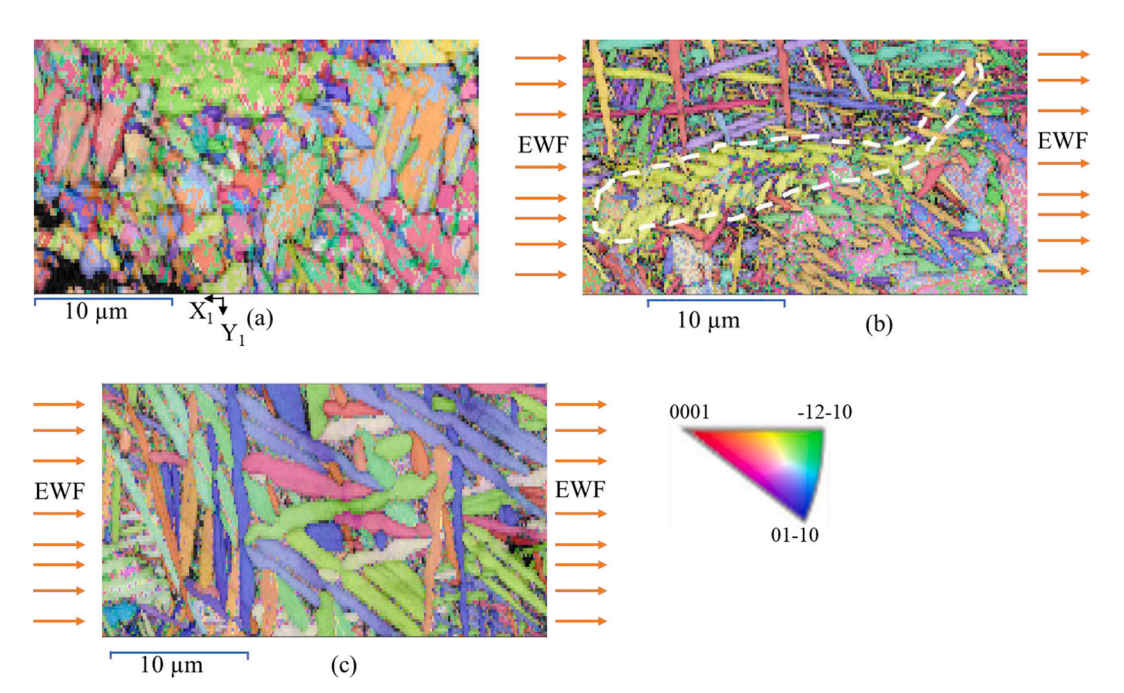


Fig. 2. zIPF maps of alloy for various processing conditions: (a) pristine; (b) pulsed at 40 °C; (c), pulsed at 120 °C, respectively. The arrows indicate the direction of electron wind force (EWF).

overall texture of ZrTi alloys and therefore their mechanical properties.

In contrast to traditional thermal annealing processes, where alpha lath structures are typically induced at higher temperatures around 500 °C [12], proposed electropulsing methodology showcases a distinct behavior. Notably, following the controlled electropulsing at a relatively modest temperature of 40 °C, a substantial increase in lath structures is observed, highlighting the unique influence of the electron wind force. Unlike conventional thermal annealing, where temperature is the primary driver of phase transformation, electropulsing introduces an additional dynamic – the electron wind force. This force, generated by the application of short pulse width and low-frequency high density current pulses, imparts mechanical momentum to the alloy, promoting enhanced atomic mobility even at lower temperatures. The micrographs, as illustrated in Fig. (2b), depict the emergence of elongated lath structures, showcasing the alloy's responsiveness to the synergistic effects of temperature variation and the electron wind force.

The altered crystallographic orientations (discussed in a later section) and the evolving microstructure emphasize the sensitivity of the alloy to even modest temperature variations and electron wind force induced by electropulsing. This microstructural evolution sets the stage for further temperature-induced changes observed in subsequent electropulsing conditions. It is to be noted that the current density is directly related to the temperature rise and electron wind force during electropulsing. According to [34], the maximum temperature rise due to a single electropulse can be expressed as:

$$\Delta T_m = \frac{t_c \rho j_m^2}{2C_0 D} \tag{1}$$

Where, t_c is the pulse width, ρ is the resistivity of the materials, C_p is the specific heat, D is the density of the materials and j_m is the current density amplitude of the applied electropulse. The controlled variation in current density within our experiment is expected to correlate directly with the temperature rise, with higher current densities contributing to more pronounced temperature increments. Although, according to Eq. (1), the temperature rise is proportional to the square of current density amplitude, it is essential to acknowledge the complexity introduced by heat exchange between the material and the environment. Table 1 presents the current densities and the corresponding recorded temperature at which the electropulsing was conducted. In addition, electron wind force is directly proportional to the applied current density [35,36]. Based on this discussion, it is expected that the increased current density in subsequent electropulsing stage will impart higher electron wind force and the associated thermal effect will also be more intense.

Fig. 2b is a representative of the initial microstructural changes due to electropulsing. It is clear that at a current density of $1.94 \times 10^4 \left(\frac{A}{cm^2}\right)$, the microstructure has evolved to fine basketweave α -lath structure. However, some of the areas were still in the original pristine condition with α -grain/broad laths. Interestingly, patches of nucleating laths (marked with white dotted boundary in Fig. 2b) were vivdly visible. Out of curiousity, we gradually increased the current density to $3.55 \times 10^4 \left(\frac{A}{cm^2}\right)$ and the temperature rose to 120 °C. This promoted extensive lath formation (Fig. 2c) with nearly the entire microstructure transforming to fine basketweave α -lath structure (please refer to the Supplementery Fig. 1 for additional maps displaying the representativeness of the alpha-lath formation). The electron wind force and

transforming to fine basketweave α -lath structure (please refer to the Supplementery Fig. 1 for additional maps displaying the representativeness of the alpha-lath formation). The electron wind force and thermal force, intensified by the higher current density, plays a pivotal role in this microstructural shift. It is to be noted that, although the EWF is inherently directional, the constraints imposed by neighboring grains hinder the formation of lath structures in a specific direction of the applied electron wind. This phenomenon occurs due to the complex interactions between neighboring grains, which may restrict the preferential orientation of lath structures along the direction of the electron

flow. Another factor is the energy requirement for grain rotation (to align in the direction of the wind force direction) and how it compares to the energy requirement for the observed phase transformation. The lenticular shape of the lath structures makes it very difficult to rotate compared to equiaxed grains [31]. In addition, grain rotation becomes energy intensive for larger grains. The combination of these factors might have led to the lath structured phase transformation with suppressed grain rotation.

A comparative analysis was performed to highlight a progressive increase in the lath structures across processing conditions. To quantify this evolution, we employed the Fiji Weka segmentation machine learning technique. Initially, a model was trained to discern and identify lath structures within the micrographs (Fig. 4a-c). This model, attuned to the distinct features of lath structures, was then applied to each condition, allowing for an assessment of the lath percentage. The subsequent quantification, facilitated by ImageJ software, revealed compelling insights into the shifting composition of lath structures. In the pristine state, the microstructure exhibited a modest $\sim 10\%$ lath content. Upon applying the first pulsing, this percentage notably increased to \sim 30%, signaling a significant growth of lath formation. However, the most striking transformation occurred after the final pulsing, where the lath content surged to \sim 90%. This systematic increase underscores the direct correlation between electropulsing conditions and the observed rise in lath structures. The temperature influence is also evident, with higher temperatures promoting more pronounced microstructural changes. In addition, another distinct characteristic, differing from that observed in standard heat treatment, is noted. Typically, in heat-treated Zr-Ti alloys, the formation of lath structures is predominantly a characteristic of the alpha-Ti (α-Ti) phase, where these lath structures precipitate into the matrix [37,38]. However, in our observations with electropulsing, we found that almost 90% of the microstructure consists of lath structures, indicating that Zirconium (Zr) also contributes to the formation of these structures under these specific conditions, a behavior not commonly seen in standard heat treatments of Zr-Ti alloys. It's noteworthy that Zr's ability to form lath structures has been observed in other scenarios, such as when alloyed with Niobium (Nb) [39].

3.2. XRD analysis on pristine and electropulsed sample

X-ray diffraction (XRD) analyses were conducted on both the pristine and final electropulsed samples to gain insight into the structural changes induced by electropulsing. The XRD pattern of the pristine sample (Fig. 5) revealed characteristic peaks consistent with the dominant alpha phases of Zr-Ti, indicative of the alloy's initial state. On examining the XRD pattern of the final electropulsed (at 120 °C) sample, a remarkable similarity in peaks was observed, affirming the persistence of alpha phases. However, a distinctive strong peak was identified at 52.5° in contrast to a weak peak for the pristine sample as shown in Fig. 5b. This peak with high intensity at 52.5° serves as compelling evidence for a pronounced increase in the density of alpha lath structures [40-42] induced by electropulsing. Arguably, this distinct peak provides a clear signature of the altered crystallographic orientation resulting from the electropulsing treatment. These observations align with the transformation "alpha to alpha-lath," reflecting the alloy's response to electropulsing. The XRD results corroborate and complement the microstructural observations, reinforcing the transformative influence of electropulsing on the alloy's structural composition.

3.3. Crystallographic orientation characteristics

The rotation of grains can lead to a change in their crystallographic orientation. This is because the crystallographic orientation of a grain is determined by the orientation of its lattice planes [43]. When a grain rotates, its lattice planes also rotate, which changes the crystallographic orientation of the grain [44]. Any changes in the pole density

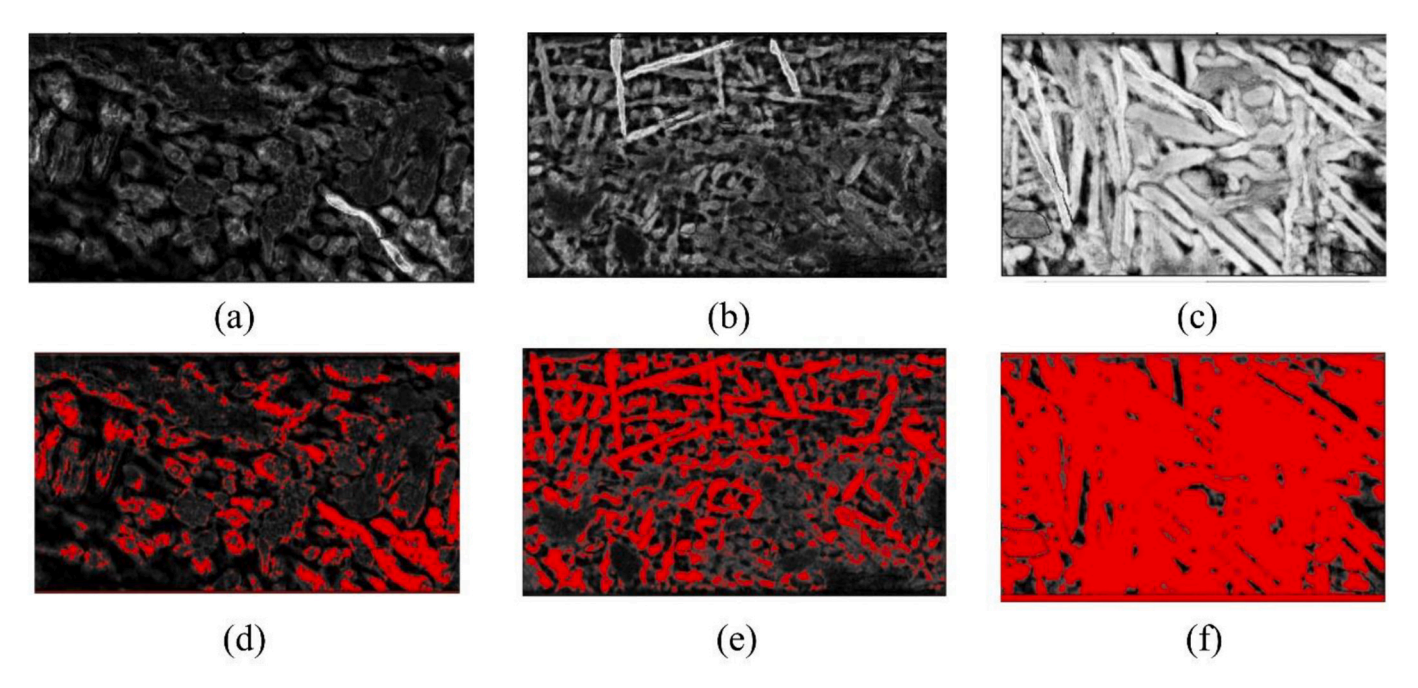
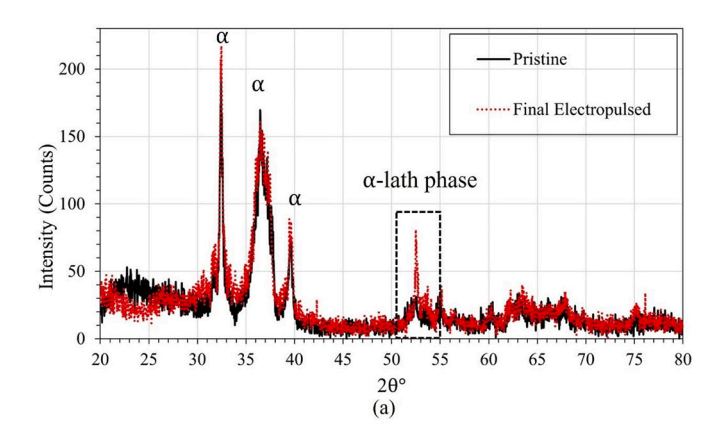


Fig. 4. Lath-structure identification (a)-(c) and quantification (d)-(f) using machine learning technique (Fiji Weka segmentation) for various processing conditions: (a), (d) pristine; (b), (e) pulsed at 40 °C; (c), (f) pulsed at 120 °C, respectively.



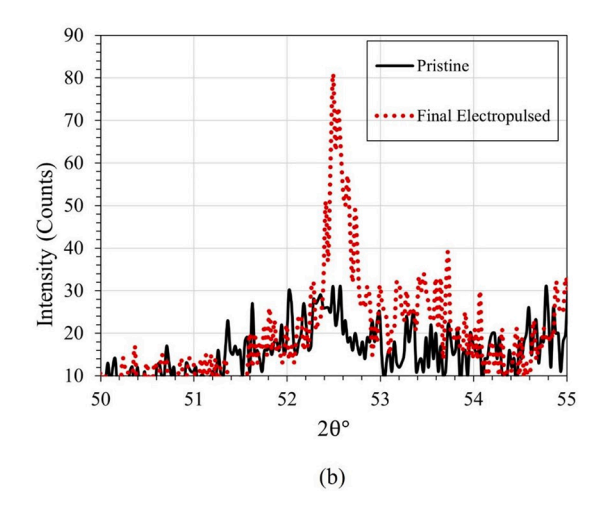


Fig. 5. (a) XRD pattern of Zr—Ti alloy; (b) Zoomed-in section highlighting the α -lath phase peak at 52.5°.

distribution imply alterations in the orientations and rotations of grains within the material. This can be illustrated by the inverse pole figure (IPF) analysis, which offers insights into the crystallographic changes induced by external factors like electropulsing. In this section, we will discuss the changes in crystallographic orientation due to electropulsing by analyzing the inverse pole figure (IPF) of the alpha phases.

In Fig. 6, the inverse pole figure (IPF) maps illustrate the crystallographic orientation evolution during distinct stages, namely the pristine state, post-electropulsing at 40 °C, and post-electropulsing at 120 °C. The IPF for the pristine sample (Fig. 6a) shows a basal texture with a $\langle 0001 \rangle$ poles normal to the surface. This suggests that the alpha grains are oriented with their $\langle 0001 \rangle //z$ -axis (i.e., perpendicular to the sample surface).

After pulsing the specimen at 40 °C (Fig. 6b), a noticeable shift of the pole density towards the $\langle -12{-}10 \rangle$ orientation was observed, signifies a change in the dominant orientation with respect to the z-axis. This shift indicates a rotation of grains in response to electropulsing. Increasing the current density in subsequent step of electropulsing leads to further rotation of the pole density towards the $\langle -12{-}10 \rangle$ orientation. This indicates a continued reorientation of grains, aligning more with this crystallographic direction. In addition, a new region of less densely distributed poles (green color) emerges towards the $\langle 01{-}10 \rangle$ orientation, suggesting additional alterations from the initial basal texture.

$\it 3.4.$ Effect of electropulsing on grain boundaries and misorientation dynamics

We further performed detailed analysis of the boundaries surrounding the α -grains/laths in the pristine and pulsed specimens. On transformating from the β phase, the α phase preserves a Burgers orientation relationship (BOR) where the {0001} basal planes of the α phase are parallel to the {110} planes of the β phase, and the closed packed $\langle 1120 \rangle$ directions of the α phase are parallel to the $\langle 111 \rangle$ directions of the β phase [45]. Based on the BOR, there are 12 possible variants for the α phase which transforms from a single parent β grain. However, due to the nucleation barrier energy associated with each variant and the impingement of these variants, only 5 distinct energetically favored α variants are reported. These include 10.53° [0001] (*Type* 6), 60° [11 $\overline{2}$ 0] (*Type* 2), 60.83° [$\overline{1.377}$ $\overline{1}$ 2.377 0.359] (*Type* 3), 63.26° [$\overline{10}$

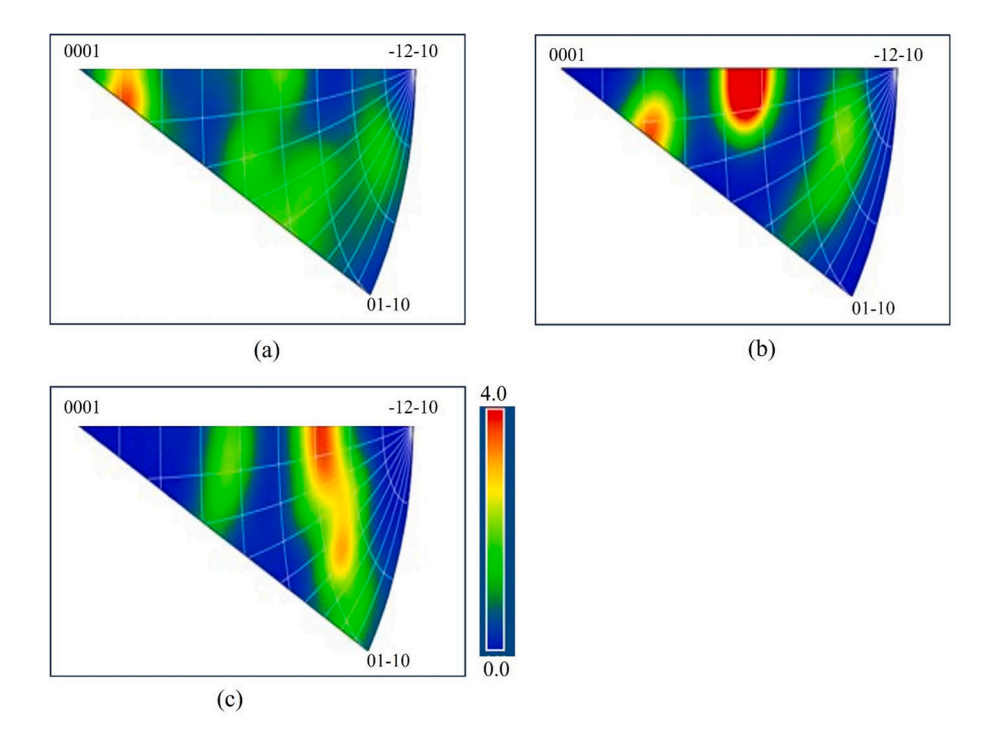


Fig. 6. Inverse pole figure distributions of hexagonal alpha phase for various conditions: (a) pristine; (b) pulsed at 40 °C; (c) pulsed at 120 °C, respectively.

5 5 3] (Type 4), and 90° [1 2.38 1.38 0] (Type 5) [46,47].

The analysis of the boundary misorientations between neighboring (correlated) α -grains/laths in the pristine and pulsed specimens (Fig. 7) agrees with the reported BOR and shows a strong peak at $60\pm5^{\circ}$, and marginal peaks at $10\pm5^{\circ}$ and $30\pm5^{\circ}$. Evidently, after pulsing, there was a progressive disappearance of the $30\pm5^{\circ}$ boundaries, and enhancement of the $60\pm5^{\circ}$ boundaries. A corresponding increase in the $10\pm5^{\circ}$ boundaries was also noted. We can postulate that the high electron wind force causes local reorientation of the microstructure. Similar results have been reported by other researchers [48].

Fig. 8 presents a detailed mapping of the special boundaries (variants based on the Burgers orientation relationship). It was clearly noted that $60^{\circ}[11\overline{2}0]$ (*Type 2*) and $60.83^{\circ}[\overline{1.377}\ \overline{1}\ 2.377\ 0.359]$ (*Type 3*) were the dominant variants in this alloy system. Initially, a few scattered boundaries of Type 2/Type 3 boundaries were present in the pristine specimen (Fig. 8a). On the contrary, pulsed specimens (Fig. 8b-c) were

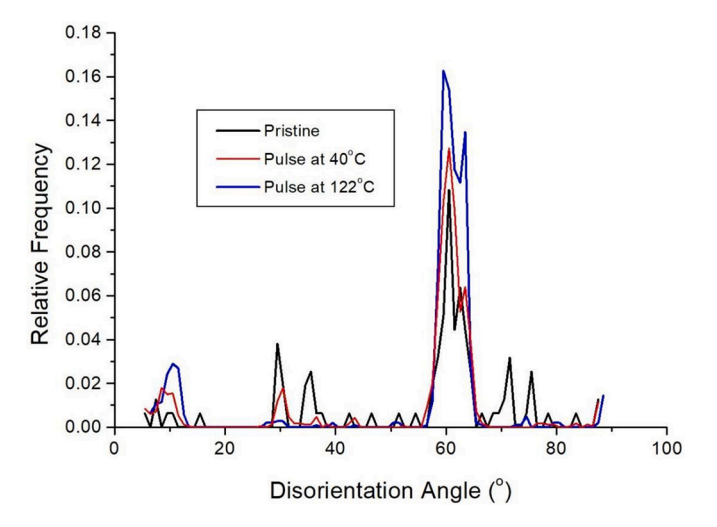


Fig. 7. Grain boundary disorientation distribution for pristine, pulsed at 40 $^{\circ}\text{C}$, and pulsed at 120 $^{\circ}\text{C}$ specimens.

populated with Type 2/Type 3 boundaries at fairly equal proportion. Meaning, these special boundaries had the same mobility and probability of growth due to the electron wind force. The high propensity of the Type 2/Type 3 boundaries matches the observed increment in the intensity of the $60 \pm 5^{\circ}$ boundaries (Fig. 7) due to electropulsing. The preferential formation of type 2 and type 3 grain boundaries, as observed in our electropulsed specimens, are critically linked to the Burgers orientation relationship inherent in the lath transformation processes within the α phase. Under conditions such as electropulsing, the electron wind force plays a pivotal role in accentuating these orientations by facilitating atomic realignment along favorable paths that conform to the Burgers orientation. This enhancement is not limited to electropulsing but is a general phenomenon observed in any treatment that leads to lath formation. The electron wind force effectively reduces the energy barriers for the nucleation of these orientations, promoting their formation at the expense of less stable configurations such as the 30° boundaries.

It should be noted that twin boundaries were observed in the pristine specimen (Fig. 8a). However, hardly any were observed in the specimen pulsed at pulsed at 1.94×10^4 $\left(\frac{A}{cn^2}\right)$ and 120 °C. This implies that the electron wind force was also capable of transforming twins to lath-structure. Twins exhibit low energy state (low dislocation density) compared to α/α '-lath structures [49]. The type 2 variant share the same rotation axis with compression twin 57.42°[11 $\overline{2}0$] at $\sim\!3^\circ$ misorientation difference. It has been reported that the 57.42°[11 $\overline{2}0$] compression twin can form via transformation from the Type 2 variant boundaries [50]. We did not observe this transformation in this study.

3.5. Impact of electropulsing on mechanical properties of Zr—Ti alloy

Nanoindentation tests were conducted at nine distinct points across the alloy, providing a comprehensive evaluation of the material's mechanical response. Fig. 9 displays the reduced modulus and hardness distribution of pristine and annealed samples. In the pristine state, the average hardness was measured at 7.03 GPa, indicating the initial mechanical strength of the alloy. Following the final annealing stage (at 120 °C), a noteworthy increase in hardness was observed, with the

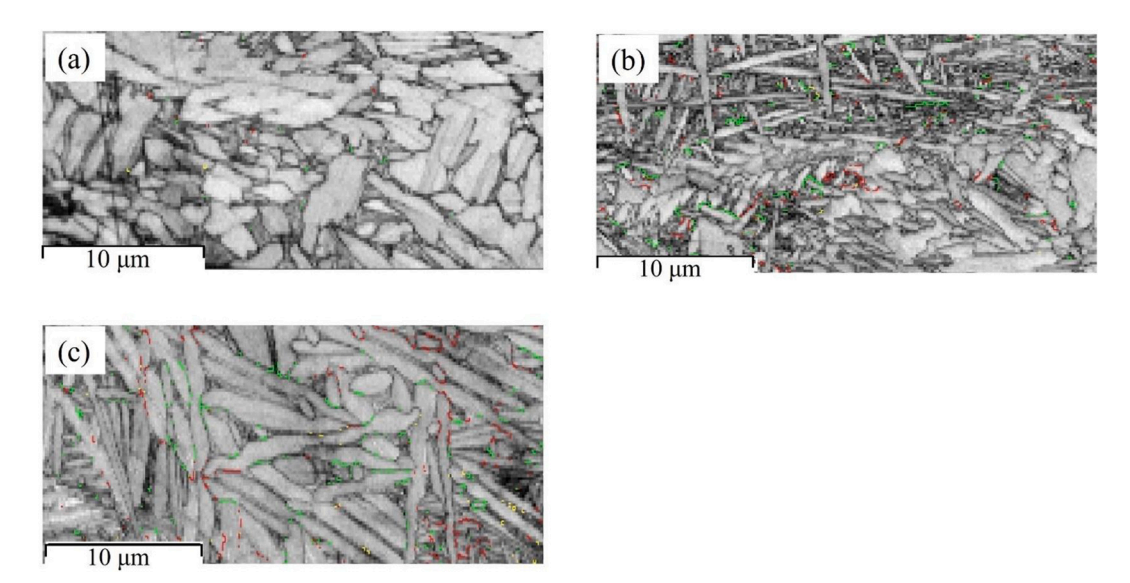


Fig. 8. Distribution of special boundaries in (a) pristine, (b) pulsed at 40 °C, and (c) pulsed at 120 °C specimens. Red boundaries are $60^{\circ}[11\overline{2}0]$ (*Type 2*) and green boundaries are $60.83^{\circ}[\overline{1.377}\ \overline{1}\ 2.377\ 0.359]$ (*Type 3*). (For interpretation of the references to color in this figure legend, the reader is referred to the web version of this article.)

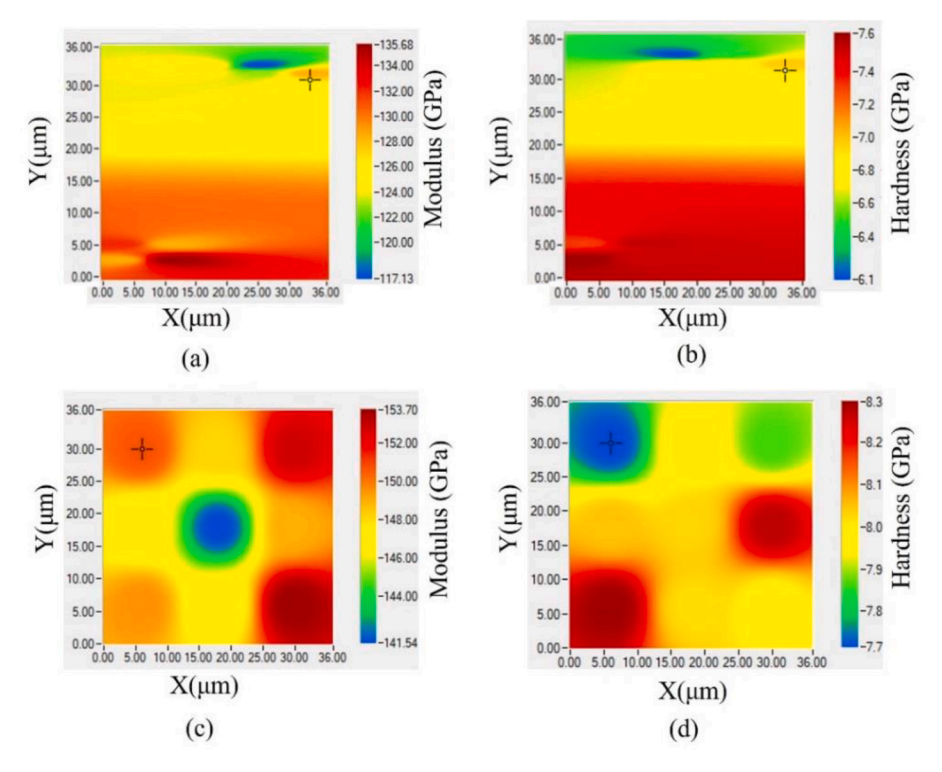


Fig. 9. Reduced modulus and hardness obtained from the nanoindentation test for pristine sample (a, c) and post pulsing at 120 °C (b, d).

average value rising to 8.02 GPa. Such increase in hardness is unexpected because α phase in titanium has lower hardness compared to the β phase [52]. However, we have discussed in earlier sections that the growth of the α -lath structure is accompanied with higher fractions of LAGBs and dislocations into the sample. The increment in the α -lath boundaries and low-angle grain boundaries (LAGBs) plays a crucial role in influencing hardness [30]. LAGBs often serve as immobile dislocation networks, acting as barriers to dislocation movement and contributing to increased material hardness [51]. These boundaries accommodate and trap dislocations, impeding their motion and hindering plastic deformation and enhance the overall hardness of the material. In

addition to higher LAGBs, the enhanced alpha-lath structure contributes to the increased hardness. Typically, alpha phase of Titanium results in lower hardness [52], however, the presence of a needle-like lath structure within the material results in a significant hardness enhancement, elevating it from $\sim\!\!7$ to $\sim\!\!8$ GPa.

In addition to hardness, the reduced modulus, representing the material's elastic stiffness, was examined. In the pristine condition, the reduced modulus was measured at 127 GPa. After electropulsing at 120 $^{\circ}$ C, the reduced modulus experienced a significant augmentation, reaching 149 GPa. This notable increase in stiffness (see Fig. 10) suggests alterations in the material's elastic behavior induced by the

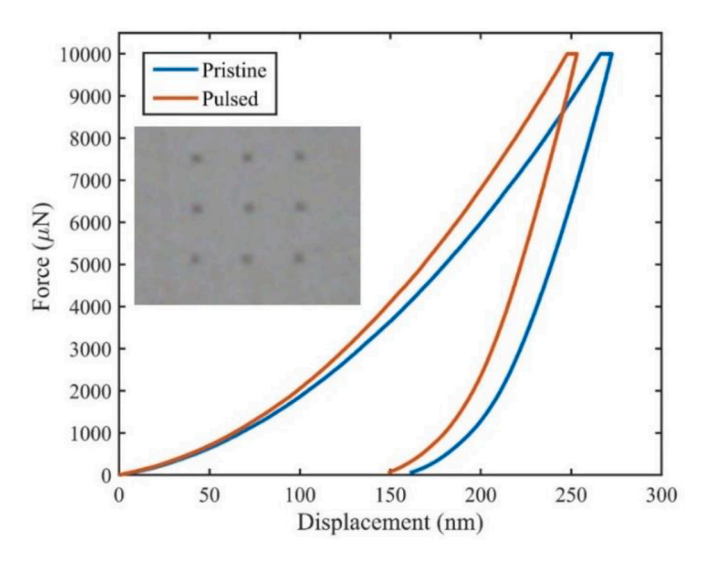


Fig. 10. Average load-displacement curves obtained by nanoindentation. The onset picture shows 9 indent points.

electropulsing process. This substantial enhancement in hardness and reduced modulus signifies the impact of electropulsing induced lath structure on the material's resistance to plastic deformation. We can postulate that the high electron wind force causes local reorientation of the microstructure to orientations that are harder or more resistant to yield. This translates to a higher external applied stress to achieve yielding for pulsed specimen than for the pristine specimen [53].

4. Conclusion

We investigated the microstructural evolution of a Zr—Ti allov subjected to electropulsing, exploring the influence of varying current density and temperature conditions. The pristine state exhibited minimal lath structure, while electropulsing at 40 °C promoted noticeable lath formation, and at 120 °C induced extensive lath structures. This unique lath structure, forming at significantly lower temperatures than conventional annealing, was characterized using techniques such as electron backscatter diffraction (EBSD), X-ray diffraction (XRD), and nanoindentation. The electropulsing process, designed to minimize thermal effects, showcased the effectiveness of electric wind force in inducing structural changes. The observed increase in lath structure was quantified through Fiji WEKA segmentation, indicating a remarkable transition from 10% to 90% lath content. Crystallographic orientation changes were elucidated through inverse pole figure (IPF) maps, revealing the rotation of grains induced by electropulsing. Additional analyses of grain boundaries and Kernel Average Misorientation (KAM) maps provided insights into the mechanical properties. We noticed significant increase in the KAM, LAGBs, and $60 \pm 5^{\circ}$ boundaries, especially Type2/Type 3 special boundaries due to electropulsing. These boundaries are barriers to dislocation motion, thereby contributing to enhanced hardness. This study sheds light on the unconventional method of electropulsing for microstructural control in Zr-Ti alloys, showcasing its potential applications in tailoring material properties for various engineering applications.

CRediT authorship contribution statement

Md Hafijur Rahman: Writing – original draft, Visualization, Validation, Methodology, Investigation. **Hajin Oh:** Validation, Methodology, Investigation. **Daudi Waryoba:** Writing – review & editing, Visualization, Validation, Supervision, Project administration, Methodology, Investigation, Funding acquisition, Formal analysis, Conceptualization. **Aman Haque:** Writing – review & editing, Validation,

Supervision, Project administration, Methodology, Investigation, Funding acquisition, Formal analysis, Conceptualization.

Declaration of competing interest

The authors declare that they have no known competing financial interests or personal relationships that could have appeared to influence the work reported in this paper.

Data availability

The raw/processed data required to reproduce these findings cannot be shared at this time due to technical or time limitations.

Acknowledgements

We acknowledge support from the US Army Research Office through award #W911NF-23-1-0359. We also acknowledge support from the Division of Materials Research, Metal & Metallic Nanostructure Program through award #2103928. Any opinions, findings, and conclusions or recommendations expressed in this material are those of the author and do not necessarily reflect the views of the sponsors.

Appendix A

Supplementary data to this article can be found online at https://doi. org/10.1016/j.matchar.2024.114188.

References

- O.N. Senkov, S. Gorsse, D.B. Miracle, High temperature strength of refractory complex concentrated alloys, Acta Mater. 175 (2019) 394–405, https://doi.org/ 10.1016/j.actamat.2019.06.032.
- [2] S.X. Liang, M.Z. Ma, R. Jing, X.Y. Zhang, R.P. Liu, Microstructure and mechanical properties of hot-rolled ZrTiAlV alloys, Mater. Sci. Eng. A 532 (2012) 1–5, https:// doi.org/10.1016/j.msea.2011.10.053
- [3] J. Li, X. Yi, K. Sun, B. Sun, W. Gao, H. Wang, X. Meng, W. Song, The effect of Zr on the transformation behaviors, microstructure and the mechanical properties of Ti-Ni-cu shape memory alloys, J. Alloys Compd. 747 (2018) 348–353, https://doi. org/10.1016/j.j.iallcom.2018.03.053
- [4] A. Misochenko, T. J V, J. Sudha, K. Padmanabhan, V. Stolyarov, Microstructure evolution and mechanical behavior in shape memory nanostructured TiNi alloy, Defect Diffus Forum. 385 (2018) 169–174, https://doi.org/10.4028/www. cciontife.pet/09.385.169
- [5] X. Li, L. Li, K. Hu, S. Qu, Vacuum brazing of TiAl-based intermetallics with Ti-Zr-Cu-Ni-Co amorphous alloy as filler metal, Intermetallics 57 (2015) 7–16, https://doi.org/10.1016/j.intermet.2014.09.010.
- [6] T. Borkar, S. Nag, Y. Ren, J. Tiley, R. Banerjee, Reactive spark plasma sintering (SPS) of nitride reinforced titanium alloy composites, J. Alloys Compd. 617 (2014) 933–945, https://doi.org/10.1016/j.jallcom.2014.08.049.
- [7] B.A. Obadele, O.S. Adesina, O.P. Oladijo, E.N. Ogunmuyiwa, Fabrication of functionally graded 316L austenitic and 2205 duplex stainless steels by spark plasma sintering, J. Alloys Compd. 849 (2020) 156697, https://doi.org/10.1016/j. iallcom 2020 156697
- [8] S. Luo, J. Luo, Q. Kang, Z. Li, G. Wang, Crystallization behavior of a Ti-Zr alloy with GH4169 alloy powder as an additive prepared via low-temperature liquid-phase spark plasma sintering, J. Mater. Eng. Perform. (2023), https://doi.org/10.1007/ s11665-023-08442-y.
- [9] C. Liu, J. Qin, Z. Feng, S. Zhang, M. Ma, X. Zhang, R. Liu, Improving the microstructure and mechanical properties of Zr-Ti alloy by nickel addition, J. Alloys Compd. 737 (2018) 405–411, https://doi.org/10.1016/j. jallcom.2017.12.046.
- [10] X. Yi, X. Feng, B. Huang, K. Sun, X. Meng, Z. Gao, Y. Zhang, H. Wang, The effect of annealing temperatures on the phase constitutes, thermal properties and corrosion behaviors of Ti-Ni-Zr-cu high entropy alloy thin ribbons, J. Alloys Compd. 896 (2022) 162947, https://doi.org/10.1016/j.jallcom.2021.162947.
- [11] C. Yi Lei, J. Zhong Mao, D. Wu Zhou, X. Min Zhang, L. Wang, Effects of annealing treatments on forming performance of zirconium alloys, Trans. Nonferrous Met. Soc. China (English Ed.) 32 (2022) 2908–2921, https://doi.org/10.1016/S1003-6326(22)65992-2.
- [12] Y. Liu, K. Chen, T. Song, B. Chen, Q. Li, C. Xia, Improvement of mechanical properties for a novel Zr–Ti–V alloy via hot-rolling and annealing treatment, Crystals 12 (2022) 1765, https://doi.org/10.3390/cryst12121765.
- [13] M.S. Khan, A. Ghatei-Kalashami, X. Wang, E. Biro, Y.N. Zhou, Refining the hierarchical structure of lath martensitic steel by in situ alloying with nickel: morphology, crystallography, and mechanical properties, J. Mater. Sci. 57 (2022) 20867–20894, https://doi.org/10.1007/s10853-022-07916-z.

- [14] R. Shu, X. Zhang, S.G. Rao, A. le Febvrier, P. Eklund, Effects of alloying and deposition temperature on phase formation and superconducting properties of TiZrTaNb-based high entropy-alloy films, Appl. Phys. Lett. 120 (2022) 151901, https://doi.org/10.1063/5.0091777.
- [15] J. Wang, W. Xiao, L. Ren, Y. Fu, C. Ma, Effect of oxygen addition and annealing time on microstructure and mechanical properties of Ti–34Nb alloy, J. Iron. Steel Res. Int. 30 (2023) 158–164, https://doi.org/10.1007/s42243-021-00707-x.
- [16] R.F. Domagala, S.R. Lyon, R. Ruh, The Pseudobinary Ti-ZrO2, J. Am. Ceram. Soc. 56 (1973) 584–587, https://doi.org/10.1111/j.1151-2916.1973.tb12421.x.
- [17] M. Szala, G. Winiarski, Ł. Wójcik, T. Bulzak, Effect of Annealing time and temperature parameters on the microstructure, hardness, and strain-hardening coefficients of 42CrMo4 Steel, Mater. (Basel, Switzerland) vol. 13 (2020), https://doi.org/10.3390/ma13092022.
- [18] X.-Q. Zha, Y. Xiong, L.-Q. Gao, X.-Y. Zhang, F.-Z. Ren, G.-X. Wang, W. Cao, Effect of annealing on microstructure and mechanical properties of cryo-rolled 316LN austenite stainless steel, Mater. Res. Express. 6 (2019) 96506, https://doi.org/ 10.1088/2053-1591/ab2a52.
- [19] J.-W. Park, H.-J. Jeong, S.-W. Jin, M.-J. Kim, K. Lee, J.J. Kim, S.-T. Hong, H.N. Han, Effect of electric current on recrystallization kinetics in interstitial free steel and AZ31 magnesium alloy, Mater Charact 133 (2017) 70–76, https://doi.org/ 10.1016/j.matchar.2017.09.021.
- [20] R.F. Zhu, J.N. Liu, G.Y. Tang, S.Q. Shi, M.W. Fu, Z.T.H. Tse, The improved superelasticity of NiTi alloy via electropulsing treatment for minutes, J. Alloys Compd. 584 (2014) 225–231, https://doi.org/10.1016/j.jallcom.2013.09.040.
- [21] Y. Zhou, W. Zhang, B. Wang, J. Guo, Ultrafine-grained microstructure in a cu–Zn alloy produced by electropulsing treatment, J. Mater. Res. 18 (2003) 1991–1997, https://doi.org/10.1557/JMR.2003.0276.
- [22] Y. Liu, J. Fan, H. Zhang, W. Jin, H. Dong, B. Xu, Recrystallization and microstructure evolution of the rolled mg-3Al-1Zn alloy strips under electropulsing treatment, J. Alloys Compd. 622 (2015) 229–235, https://doi.org/ 10.1016/j.jallcom.2014.10.062.
- [23] J.-H. Roh, J.-J. Seo, S.-T. Hong, M.-J. Kim, H.N. Han, J.T. Roth, The mechanical behavior of 5052-H32 aluminum alloys under a pulsed electric current, Int. J. Plast. 58 (2014) 84–99, https://doi.org/10.1016/j.iiplas.2014.02.002.
- [24] Y. Zhu, S. To, X. Liu, G. Hu, Effect of static electropulsing on microstructure and elongation of a Zn-Al alloy (ZA22), Metall. Mater. Trans. A Phys. Metall. Mater. Sci. 42 (2011) 1933–1940, https://doi.org/10.1007/s11661-010-0591-x.
- [25] Z.N. Yang, F. Jiang, X.B. Wang, L. Qu, Y.G. Li, L.J. Chai, F.C. Zhang, Effect of electropulsing treatment on microstructure and mechanical properties of a Deformed ZrTiAlV Alloy, Mater. (Basel, Switzerland) vol. 12 (2019) 3560, https:// doi.org/10.3390/ma12213560.
- [26] A. Yamaguchi, S. Nasu, H. Tanigawa, T. Ono, K. Miyake, K. Mibu, T. Shinjo, Effect of joule heating in current-driven domain wall motion, Appl. Phys. Lett. 86 (2004) 12511, https://doi.org/10.1063/1.1847714.
- [27] M. Mecklenburg, B.T. Zutter, X.Y. Ling, W.A. Hubbard, B.C. Regan, Visualizing the Electron wind force in the elastic regime, Nano Lett. 21 (2021) 10172–10177, https://doi.org/10.1021/acs.nanolett.102641.
- [28] M.-J. Kim, K. Lee, K.H. Oh, I.-S. Choi, H.-H. Yu, S.-T. Hong, H.N. Han, Electric current-induced annealing during uniaxial tension of aluminum alloy, Scr. Mater. 75 (2014) 58–61, https://doi.org/10.1016/j.scriptamat.2013.11.019.
- [29] M.-J. Kim, M.-G. Lee, K. Hariharan, S.-T. Hong, I.-S. Choi, D. Kim, K.H. Oh, H. N. Han, Electric current—assisted deformation behavior of Al-mg-Si alloy under uniaxial tension, Int. J. Plast. 94 (2017) 148–170, https://doi.org/10.1016/j.iiplas.2016.09.010.
- [30] A. Haque, J. Sherbondy, D. Warywoba, P. Hsu, S. Roy, Room-temperature stress reduction in welded joints through electropulsing, J. Mater. Process. Technol. 299 (2022) 117391, https://doi.org/10.1016/j.jmatprotec.2021.117391.
- [31] M.H. Rahman, H. Oh, D. Waryoba, A. Haque, Room temperature control of grain orientation via directionally modulated current pulses, Mater. Res. Express. 10 (2023) 116521. http://iopscience.iop.org/article/10.1088/2053-1591/ad0b56.
- [32] M.H. Rahman, S. Todaro, L. Warner, D. Waryoba, A. Haque, Elimination of low-angle grain boundary networks in FeCrAl alloys with the Electron wind force at a low temperature, Metals (Basel). 14 (2024) 331, https://doi.org/10.3390/pps14090321
- [33] P. Trimby, I. Anderson, K. Larsen, M. Hjelmstad, K. Thomsen, K. Mehnert, Advanced classification of microstructures in EBSD datasets using AZtecCrystal,

- Microsc. Microanal. 26 (2020) 1–2, https://doi.org/10.1017/ \$1431927620013410
- [34] R. Wang, Z. Xu, Y. Jiang, G. Tang, J. Wan, K.J.-C. Zhenqian Chou Zhou, Q. Li, The coupling of thermal and athermal effect in high-density multiple pulse continuous treatment of AZ31, Mater. Des. 215 (2022) 110495, https://doi.org/10.1016/j.matdes.2022.110495
- [35] D. Waryoba, Z. Islam, B. Wang, A. Haque, Low temperature annealing of metals with electrical wind force effects, J. Mater. Sci. Technol. 35 (2019) 465–472, https://doi.org/10.1016/j.jmst.2018.09.069.
- [36] S.J. Hoving, A. Lodder, R.S. Sorbello, Finite-cluster description of electromigration, Phys. Rev. B Condens. Matter 25 (1982) 6178–6187.
- [37] J. Cheng, S. Yu, J. Li, J. Gai, Z. Du, F. Dong, J. Zhang, X. Zhang, Precipitation behavior and microstructural evolution of α phase during hot deformation in a novel β-air-cooled metastable β-type Ti-B12 alloy, Metals (Basel). 12 (2022), https://doi.org/10.3390/met12050770.
- [38] B. He, J. Sun, Y. Ren, C. Li, G. Yang, X. Li, J. Ni, Effect of heat treatment on microstructure and mechanical properties of laser-deposited Ti65 near-alpha titanium alloy, J. Mater. Res. 37 (2022), https://doi.org/10.1557/s43578-022-00547-0
- [39] R. Kondo, N. Nomura, Y. Suyalatu, H. Tsutsumi, T. Hanawa Doi, Microstructure and mechanical properties of as-cast Zr–Nb alloys, Acta Biomater. 7 (2011) 4278–4284, https://doi.org/10.1016/j.actbio.2011.07.020.
- [40] M. Takahashi, M. Kikuchi, O. Okuno, Grindability of dental cast Ti-Zr alloys, Mater. Trans. 50 (2009) 859–863, https://doi.org/10.2320/matertrans.MRA2008403.
- [41] T. Shiraishi, K. Yubuta, T. Shishido, N. Shinozaki, Elastic properties of as-solidified Ti-Zr binary alloys for biomedical applications, Mater. Trans. 57 (2016) 1986–1992, https://doi.org/10.2320/matertrans.MI201501.
- [42] H. Dong, Z. Feng, S. Liang, X. Sun, J. Li, D. Wu, R. Su, X. Zhang, Evolution of microstructure, mechanical properties and corrosion behaviors using cooling rate regulation in a novel ZrTi-based alloy, J. Mater. Res. Technol. 9 (2020) 3471–3480, https://doi.org/10.1016/j.jmrt.2020.01.084.
- [43] X. Wang, S. Gao, E. Jain, B. Gaskey, M. Seita, Measuring crystal orientation from etched surfaces via directional reflectance microscopy, J. Mater. Sci. 55 (2020) 11669–11678, https://doi.org/10.1007/s10853-020-04734-z.
- [44] L. Wang, J. Teng, P. Liu, A. Hirata, E. Ma, Z. Zhang, M. Chen, X. Han, Grain rotation mediated by grain boundary dislocations in nanocrystalline platinum, Nat. Commun. 5 (2014) 4402. https://doi.org/10.1038/ncomms5402.
- [45] W.G. Burgers, On the process of transition of the cubic-body-centered modification into the hexagonal-close-packed modification of zirconium, Physica 1 (1934) 561–586, https://doi.org/10.1016/S0031-8914(34)80244-3.
- [46] T. Karthikeyan, S. Saroja, M. Vijayalakshmi, Evaluation of misorientation angleaxis set between variants during transformation of bcc to hcp phase obeying Burgers orientation relation, Scr. Mater. 55 (2006) 771–774, https://doi.org/ 10.1016/i.scr.intamat.2006.07.022.
- [47] N. Gey, M. Humbert, Specific analysis of EBSD data to study the texture inheritance due to the β → α phase transformation, J. Mater. Sci. 38 (2003) 1289–1294, https://doi.org/10.1023/A:1022842712172.
- [48] J. Kuang, X. Du, X. Li, Y. Yanyang, A. Luo, G. Tang, Athermal influence of pulsed electric current on the twinning behavior of Mg-3Al-1Zn alloy during rolling, Scr. Mater. 114 (2016) 151-155.
- [49] X. Yan, X. Xu, Y. Zhao, Y. Zhou, Z. Wu, L. Wei, Y. Yu, C. Wu, Variant selection induced by electropulsing: optimization in the microstructure of selective laser melted Ti-6Al-4 V alloy, J. Mater. Sci. Technol. 159 (2023) 219–224, https://doi. org/10.1016/j.jmst.2023.03.015.
- [50] R. Ma, X. Zhang, Improvement of mechanical properties and microstructural refining of cast titanium alloys by coupling of electropulsing and temporary alloying element hydrogen, Mater. Sci. Eng. A 858 (2022) 144176, https://doi.org/ 10.1016/j.msea.2022.144176
- [51] F. Javaid, Y. Xu, K. Durst, Local analysis on dislocation structure and hardening during grain boundary pop-ins in tungsten, J. Mater. Sci. 55 (2020) 9597–9607, https://doi.org/10.1007/s10853-020-04655-x.
- [52] A. Gupta, G. Shankar, D. Mahadule, R.K. Khatirkar, Correlation of alpha phase and its texture stability in heat-treated Ti-6.5%Al-4.4%V-0.15%Fe alloy, J. Mater. Eng. Perform. 32 (2023) 9599–9613, https://doi.org/10.1007/s11665-023-07811-x.
- [53] Y. Liu, S. Lin, S.-J. Chiu, On the Schmid's law for the electric current-induced deformation: an in situ EBSD study, Int. J. Mech. Sci. 168 (2019) 105295, https://doi.org/10.1016/j.ijmecsci.2019.105295.